

A mechanistic analysis of stone fracture in lithotripsy

Oleg A. Sapozhnikov

Department of Acoustics, Physics Faculty, Moscow State University, Leninskie Gory, Moscow, 119992, Russia

Adam D. Maxwell, Brian MacConaghy, and Michael R. Bailey^{a)}

Center for Industrial and Medical Ultrasound, Applied Physics Laboratory, University of Washington, 1013 Northeast 40th Street, Seattle, Washington 98105

(Received 17 July 2006; revised 7 November 2006; accepted 9 November 2006)

In vitro experiments and an elastic wave model were used to analyze how stress is induced in kidney stones by lithotripsy and to test the roles of individual mechanisms—spallation, squeezing, and cavitation. Cylindrical U30 cement stones were treated in an HM-3-style lithotripter. Baffles were used to block specific waves responsible for spallation or squeezing. Stones with and without surface cracks added to simulate cavitation damage were tested in glycerol (a cavitation suppressive medium). Each case was simulated using the elasticity equations for an isotropic medium. The calculated location of maximum stress compared well with the experimental observations of where stones fractured in two pieces. Higher calculated maximum tensile stress correlated with fewer shock waves required for fracture. The highest calculated tensile stresses resulted from shear waves initiated at the proximal corners and strengthened along the side surfaces of the stone by the liquid-borne lithotripter shock wave. Peak tensile stress was in the distal end of the stone where fracture occurred. Reflection of the longitudinal wave from the distal face of the stone—spallation—produced lower stresses. Surface cracks accelerated fragmentation when created near the location where the maximum stress was predicted. © 2007 Acoustical Society of America.

[DOI: 10.1121/1.2404894]

PACS number(s): 43.80.Gx [CCC]

Pages: 1190–1202

I. INTRODUCTION

Despite over 20 years of clinical practice and fundamental research, a complete physical explanation of stone comminution by lithotripsy remains unknown. Incomplete understanding is evidenced by rising retreatment rates despite the release of over 40 lithotripter designs over the history of shock wave lithotripsy (SWL).^{1–3} The goal of this paper is to explain how a specific stone fractures by using a theoretical model to simulate the combined effect of many mechanisms and by using the model and experiment to test the role of individual already-described mechanisms of inducing the stress that leads to stone fracture.

Stone fracture is similar to fracture of any brittle object and can be considered as a process whereby cracks form, grow, and coalesce as a result of internal stresses, in this case, generated by the externally applied lithotripter shock wave (Fig. 1). Cracks are presumed to initiate at locations where the stress exceeds a critical value. Cracks grow and coalesce under the repetitive loading and unloading in a process called dynamic fatigue, and common practice indicates several lithotripter shock waves are required to fracture stones.⁴ Generally, the process of crack growth can be studied using existing methods of fracture mechanics, for instance, using the cohesive zone model.^{5–7} Although the described scenario of fracture is agreed upon, this knowledge in

itself does not help in predicting stone fragmentation without knowing the mechanisms of how appropriate stresses are generated inside the stone.

A. Direct physical mechanisms of shock-wave-induced stress

Several physical mechanisms, i.e., ways stresses leading to stone fracture are generated, have been proposed, but there is no consensus on the roles of these various mechanisms. The two primary mechanisms directly resulting from the shock wave (SW) and investigated here are spallation due to reflections of longitudinal waves within the stone^{8,9} and squeezing due to circumferential stresses generated by shock waves outside the stone.¹⁰

In spallation, the distal surface of a stone in liquid or tissue is an acoustically soft interface, generating a reflected tensile wave from the initially compressive longitudinal shock pulse (Fig. 1) that enters and propagates through the stone.¹¹ With a flat distal surface, spallation yields a maximum tension within the stone where the reflected tensile wave overlaps the negative tail (Fig. 1) of the incident wave; the distance of this maximum from the distal surface, l , is fixed by the pulse length alone: $l = c_l \Delta t / 2$, where c_l is longitudinal wave speed in the stone and Δt is time delay between the positive and negative peaks in the acoustic waveform. For instance, if $c_l = 3 \text{ mm}/\mu\text{s}$ (typical value for kidney stones), then for the waveform of Fig. 1 that has $\Delta t \approx 2 \mu\text{s}$, this formula predicts $l \approx 3 \text{ mm}$, which is close to the experimental observations. The predicted spall-formed failure sur-

^{a)}Electronic mail: bailey@apl.washington.edu

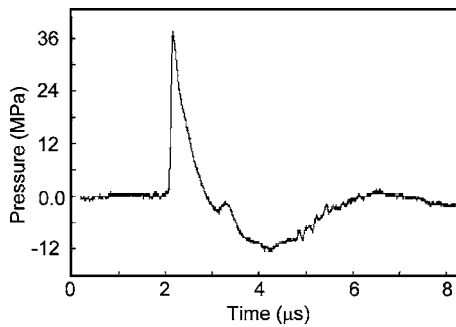


FIG. 1. Shock wave generated by an HM-3-clone lithotripter and measured by PVDF membrane hydrophone in water. An initial positive pressure spike of $1 \mu\text{s}$ is followed by a negative pressure trough of roughly $4 \mu\text{s}$.

face is orthogonal to the shock wave propagation and appears close to the distal surface of the stone. With a curved distal stone surface, the position of the maximum depends on the curvature, and the maximum can be intensified by focusing of the reflected wave.^{12–14}

In squeezing, the shock wave is assumed to be broader but shorter than the stone and travels in liquid along the side surface of the stone creating circumferential stress on the stone.¹⁰ Eisenmenger¹⁰ supposed that the wave velocity in the fluid is much lower than the elastic wave velocities in the stone, i.e., the longitudinal wave moves through the stone leaving the thin shock wave in the fluid encircling and squeezing the stone in a quasi-static manner. As a result, tensile stresses are created near the proximal and distal ends of the stone, which gives rise to a fracture parallel to the wave-propagation direction.

There is experimental evidence for both mechanisms. The spallation mechanism is supported by the fact that generally stones appear to break first in two pieces with the fracture in the distal end of the stone. Figure 2 shows a typical break for a cylindrical U30 model stone.¹⁵ A fracture occurred about one-third of the length from the distal end and has frequently been attributed to spallation.^{8,9,16} A lithotripter designed to emphasize the squeezing mechanism with a broad (less-focused) shock wave that extends laterally well beyond the width of the stone has been shown to be clinically efficacious,¹⁷ and modeling shows squeezing could account for the observed fracturing in half of stones.^{10,18} Nei-



FIG. 2. (Color online) Typical fracture pattern for a U30 model stone treated fixed at the focus of an HM-3 clone lithotripter. The proximal face (left) has cavitation pitting. The stone is fractured in two pieces about $1/3$ of the length from the distal end.

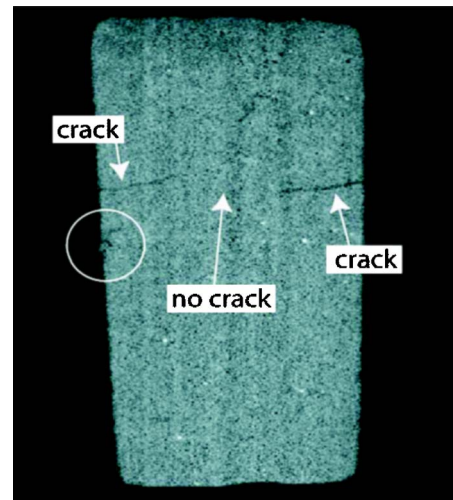


FIG. 3. (Color online) Micro-computed tomography image of a U30 model stone treated in an HM-3-clone lithotripter before the stone fractured in two pieces. Cracks are apparent extending outside of the stone toward the axis of the stone at about $1/3$ of the length from the distal end. Used with permission from Robin Cleveland (Ref. 25).

ther mechanism alone explains both these results, which supports either a combination of these two mechanisms or a separate mechanism.

B. Indirect physical mechanisms of shock-wave-induced stress

In addition to the direct mechanisms, the lithotripter produces cavitation that can generate stress in the stone and cause fracture.¹⁹ Cavitation—of individual bubbles or clusters of bubbles in fluid near the stone surface—creates localized pressure and stress waves that diverge. Localized stress initiated at the stone surface can be created by direct impact of a fluid jet formed by asymmetric bubble or cloud collapse, and stress can be created by SWs generated by asymmetric or symmetric collapse. SWs are generated by the halting of the intruding fluid by the compressed contents of a symmetric bubble or by the water jet forcibly impinging the fluid on the opposite side of an asymmetric bubble. These SWs can have much higher peak pressures than the lithotripter shock wave; however, individual collapse emissions are spherically diverging and lose amplitude rapidly with propagation distance.²⁰ Cavitation, by these mechanisms, induces stress at a localized region on the stone surface.

As with the direct mechanisms, there is substantial evidence cavitation plays a role in stone comminution in SWL. Stones have been shown not to fragment when cavitation is suppressed by static pressure,²¹ viscous fluid,²² or shock wave modification.^{23,24} Pits and fractures in the proximal face of the stone (Fig. 2) have commonly been attributed to cavitation. Here, we focus on the fracture in two pieces at the distal surface. X-ray computed tomography images of U30 model stones treated in a Dornier HM-3-clone lithotripter indicate that these fractures grow from the surface of the stone inward (Fig 3).²⁵ Pishchalnikov *et al.*,²⁶ with a similar HM-3-clone lithotripter, observed not only a substantial jet through a large cavitation cluster on the proximal face of the U30 stone but a ring of bubbles around the stone near the

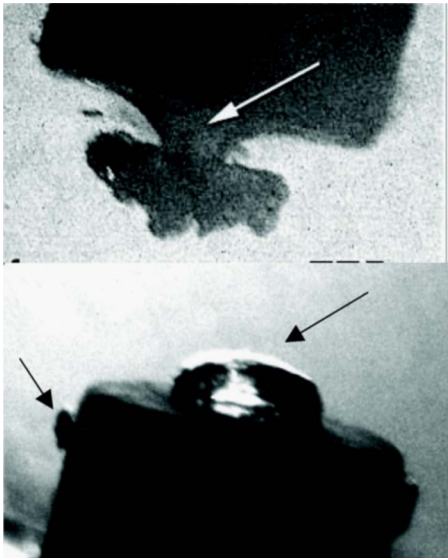


FIG. 4. (Color online) High-speed photography of the cavitation clouds on the proximal end (top) and distal end (bottom) of a U30 stone following passage of a lithotripter SW. Entrained bubbles reveal the fluid jet impinging on the proximal surface as the cloud collapses. A band of bubbles can be seen encircling the stone near where cracks are seen in Fig. 3 and where fracture occurred in Fig. 2. Used with permission from the Journal of Endourology (Ref. 26).

distal end (Fig. 4). The jet was approximately 1 mm in diameter, and other evidence indicates jet velocities can reach 100 m/s.^{27,28} Spherically diverging shock waves resulting from bubble collapse were observed with shadowgraph imaging. Experiments also showed that cracks were generated at the proximal and side surfaces. Sapozhnikov *et al.*²⁹ used the linear elasticity model described in this paper to determine that elastic waves in the stone created a low pressure that encircled the stone near the distal end. This low pressure yielded a particularly long growth and collapse cycle in a single bubble modeled with the Gilmore equation,^{20,30} and was therefore used to explain the existence of the cloud ring encircling the stone. It is not known whether the cavitation collapse on the proximal surface imparts stress that leads to fracture of the distal end or if pitting by the cavitation ring contributes to this fracture.

C. Effort to model stone comminution in SWL

Numerical models reveal information perhaps not detected in experiments and make possible parametric studies of the effect of variables difficult or time-consuming to control in experiments. For example, the following models developed specifically for application to SWL have been used to simulate effects of varying the shock wave delivery rate, numbers of cavitation bubbles, stone shape, stone material, lithotripter waveform, and beamwidth. Tanguay and Colonius³¹ have coupled a prediction of the acoustic field with a model of the bubble cloud behavior near a rigid stone surface, and predicted an optimal shock wave delivery rate. Zabolotskaya *et al.*³² have focused on the bubble-bubble interactions near a rigid stone. Dahake and Gracewski^{12,13} developed a linear elastic model of stress waves within the stone that they tested against spherical and oval model

stones. LeVeque³³ has coupled nonlinear acoustic and nonlinear elastic models in what is called CLAWPACK and has reported initial results of medical shock wave interaction with bones. Cleveland and Sapozhnikov¹⁸ recently modified the linear elastic approach in order to pinpoint the location of maximum stress for comparison with the location of initial fracture in model stones.

D. Scope of this paper

In this paper, action of a shock wave on a stone is studied using a finite difference model in the approximation of linear elasticity, and by visual observation of fracture in U30 model stones. First, the theoretical model is used to describe as a whole the mechanisms involved in producing the maximum stress in the stone. Second, the role of individual mechanisms is tested numerically and experimentally. The end point of the experiments was fracture of the stone into two pieces as shown in Fig. 2 or a predetermined maximum number of SWs without fracture. Location of the calculated maximum stress is compared to the location of fracture determined experimentally, and relative amplitude of the maximum stress is compared to number of SWs to fracture. The scope is restricted to the first fracture into two pieces, not full comminution, of a specific stone model of one shape and composition. If suppressing one mechanism did not cause an increase in the SWs required for fracture, it was interpreted that the mechanism was of lesser importance and could not alone explain the fracture. The following hypotheses were tested.

If spallation is the sole mechanism: Stones will fracture at the distal end as shown in Fig. 2 (Spallation Test 1). Stones of different length will fracture the same distance from the distal end (Spallation Test 2). Blocking transmission of the SW through most of the proximal face will increase the number of SWs to fracture (Spallation Test 3).

If squeezing is the sole mechanism: Blocking transmission of the squeezing wave will increase the number of SWs to fracture (Squeezing Test 1). The shape of the tip or the tail of the stone will not alter the number of SWs to fracture (Squeezing Test 2). Blocking the entire proximal face of the stone will not alter the number of SWs to fracture (Squeezing Test 3).

If cavitation is the sole mechanism: Jet impact will produce high stress in the region of fracture (Cavitation Test 1).

If cracks formed by cavitation are significant in fracture: Stones in a cavitation suppressing medium will have a higher number of SWs to fracture than stones in a cavitating medium (Cavitation Test 2). Stones with surface cracks but in a cavitation suppressing medium will have the same number of SWs to fracture as stones initially without surface cracks in a cavitation supporting medium (Cavitation Test 3).

II. THEORY

A. Description of the model

A linear elastic model was used to simulate the stress wave propagation within a kidney stone. The model is described in the paper by Cleveland and Sapozhnikov.¹⁸ Here,

we summarize the model, list the material properties used, and describe the predicted parameters to be compared to experiment.

Kidney stones exhibit a brittle behavior, i.e., little or no visible plastic deformation precedes the fracture;^{7,34} therefore, linear elasticity is a reasonable model to the point of stone failure. The stone and surrounding liquid are considered as an isotropic medium. The dynamics of such a medium is governed by the equation of motion

$$\rho \frac{\partial v_i}{\partial t} = \frac{\partial \sigma_{ij}}{\partial x_j}, \quad (1)$$

where $i, j=1, 2, 3$, ρ is medium density, $v_i = \partial u_i / \partial t$ are medium velocity components (u_i are displacement vector components), and σ_{ij} are components of stress tensor. In the linear approximation, that is valid for small strains, elastic forces are governed by Hooke's law:

$$\sigma_{ij} = \lambda (\nabla \cdot \mathbf{u}) \delta_{ij} + \mu \left(\frac{\partial u_i}{\partial x_j} + \frac{\partial u_j}{\partial x_i} \right). \quad (2)$$

Here λ and μ are the Lamé constants (μ is also called the shear modulus), and δ_{ij} is the Kronecker delta function. Note that the stress tensor is symmetric: $\sigma_{ij} = \sigma_{ji}$, i.e., only six of the nine tensor components are independent. We suppose that the stone has an axisymmetric shape with the axis oriented along the initial shock wave propagation. It is convenient to use polar coordinates (r, z, θ) , where r and z are the radial and axial distances and θ is the polar angle. Because of the axial symmetry of the problem, the velocity vector has only two components—radial, v_r , and axial, v_z , and only four stress tensor components are nonzero: σ_{rr} , σ_{zz} , $\sigma_{\theta\theta}$, and σ_{rz} . Equations (1) and (2) can be written in the following form suitable for the numerical implementation:

$$\frac{\partial v_r}{\partial t} = \rho^{-1} \left\{ \frac{1}{r} \frac{\partial [r(\sigma_{rr} - \sigma_{\theta\theta})]}{\partial r} + \frac{\partial \sigma_{rz}}{\partial z} + \frac{\partial \sigma_{\theta\theta}}{\partial r} \right\}, \quad (3)$$

$$\frac{\partial v_z}{\partial t} = \rho^{-1} \left\{ \frac{1}{r} \frac{\partial (r\sigma_{rz})}{\partial r} + \frac{\partial \sigma_{zz}}{\partial z} \right\}, \quad (4)$$

$$\frac{\partial \sigma_{rr}}{\partial t} = \lambda \left(\frac{1}{r} \frac{\partial (rv_r)}{\partial r} + \frac{\partial v_z}{\partial z} \right) + 2\mu \frac{\partial v_r}{\partial r}, \quad (5)$$

$$\frac{\partial \sigma_{zz}}{\partial t} = \lambda \frac{1}{r} \frac{\partial (rv_r)}{\partial r} + (\lambda + 2\mu) \frac{\partial v_z}{\partial z}, \quad (6)$$

$$\frac{\partial \sigma_{\theta\theta}}{\partial t} = \lambda \frac{\partial v_z}{\partial z} + (\lambda + 2\mu) \frac{1}{r} \frac{\partial (rv_r)}{\partial r} - 2\mu \frac{\partial v_r}{\partial r}, \quad (7)$$

$$\frac{\partial \sigma_{rz}}{\partial t} = \mu \left(\frac{\partial v_z}{\partial r} + \frac{\partial v_r}{\partial z} \right). \quad (8)$$

When the stone is surrounded by liquid, appropriate boundary conditions should be used for velocities and forces. However, it is more convenient and valid to consider the liquid and stone as one inhomogeneous medium whose parameters ρ , λ , and μ are functions of the spatial coordinates. In this approach there is no need to consider the stone bound-

ary separately, i.e., the boundary conditions are accounted for automatically.¹⁸ This approach also allows introducing inhomogeneity to the stone structure. Here, only uniform U30 stones are modeled and the physical properties are density $\rho = 1700 \text{ kg/m}^3$, longitudinal sound speed $c_l = [(\lambda + 2\mu)/\rho]^{1/2} = 2630 \text{ m/s}$, shear wave speed $c_s = (\mu/\rho)^{1/2} = 1330 \text{ m/s}$, which corresponds to $\lambda = 5.8 \text{ GPa}$, and $\mu = 3.9 \text{ GPa}$. Values for water are $\rho = 1000 \text{ kg/m}^3$, sound speed in liquid $c_l = 1500 \text{ m/s}$, and $\lambda = 2.25 \text{ GPa}$.¹⁸ Water is assumed not to support shear: $\mu = 0$. All calculations are lossless.

To solve Eqs. (3)–(8) in finite differences, the partial differential equations are discretized using a central differencing scheme with staggered grids both in space and in time.^{18,35} Velocity and stress in the stone are initially set to zero. The initial conditions in the liquid correspond to the traveling shock pulse. Although arbitrary initial pressure distribution is possible, in this paper we suppose that the initial pulse is a plane wave. This approximation is supported by the existence of a Mach stem during weak shock focusing in a Dornier HM3 lithotripter.⁴ It is supposed that a lithotripter shock wave is initially located in the liquid 5 mm to the left of the stone and propagates to the right as a plane wave. For such a plane wave, $\sigma_{rr} = \sigma_{zz} = \sigma_{\theta\theta} = -P(t + (z_* - z)/c_l)$, $\sigma_{rz} = 0$, $v_r = 0$, and $v_z = (\rho c_l)^{-1} P(t + (z_* - z)/c_l)$. The acoustic pressure waveform $P(t)$ at the initial position $z = z_*$ was a classic lithotripsy pulse modified with a hyperbolic tangent function to provide a smooth shock front:²⁰ $P(t) = (P_0/2)[1 + \tanh(t/t_s)] \exp(-t/t_L) \cos(2\pi f_L t + \pi/3)$, where P_0 is peak pressure, t_s is the shock front thickness, and $t_L = 1.1 \mu\text{s}$ and $f_L = 83.3 \text{ kHz}$ control the pressure waveform. The wave is an analytical approximation to the measured wave shown in Fig. 1. We used $P_0 = 50 \text{ MPa}$, which is roughly the amplitude produced by our lithotripter,³⁶ and $t_s = 100 \text{ ns}$, which is the rise-time measured *in vivo*.³⁷

Elastic waves in a cylindrical U30 stone with diameter 6.5 mm and length 8.5 mm were modeled. The calculation region was a cylinder of 20 mm diameter and 30 mm length, and calculations were completed before reflections from the region boundary reached the stone. The typical spatial grid step was $h_z = h_r = 50 \mu\text{m}$ and the temporal step was $h_t = 0.5 h_z / c_l \approx 10 \text{ ns}$, which was sufficient to maintain stability and accuracy.

In this paper, the maximum principal tensile stress is the value reported. In the considered axisymmetric case, the three principal stresses are: $\sigma_{I,II} = (\sigma_{zz} + \sigma_{rr}) / 2 \pm \sqrt{((\sigma_{zz} - \sigma_{rr})/2)^2 + \sigma_{rz}^2}$ and $\sigma_{III} = \sigma_{\theta\theta}$. The maximum principal tensile stress $\sigma_{\max} = \max(\sigma_I, \sigma_{III})$ is an appropriate parameter to characterize shock wave impact on kidney stones, because brittle materials, such as kidney stones, are typically weakest in tension. Calculated results reported here show σ_{\max} on a discretized slice of the stone at a snapshot in time, for various subsequent times. The stress σ_{\max} is plotted on a fixed scale blue -70 MPa to red $+70 \text{ MPa}$, where minus indicates compression. In the on-line version color images are used on a scale blue -70 MPa to red $+70 \text{ MPa}$. The stress field at the instant of peak σ_{\max} is referred to as the peak stress field. The field plotted as the maximum tension recorded over the duration of the simulation at each location in the stone is referred to as the max field and indicates where

the highest tension occurred. Other relevant parameters such as maximum strain or maximum shear stress do not produce markedly different stress field maps.¹⁸ To aid interpretation of the results, the divergence of the particle velocity was used to identify waves traveling at the longitudinal wave speed, and the curl of the particle velocity was used to identify waves at the shear wave speed.¹⁸

B. Test of mechanisms

Table I shows the simulated experiments conducted to test the nine hypotheses. Diameter of the cylindrical portion of all stones was 6.5 mm. Acoustically reflective disks and baffles were simulated as pressure release media with low wave velocities: $c_l=3$ m/s and $c_l=1.5$ m/s. For Cavitation Test 1, a 1-mm-diam cylinder of fluid with velocity 100 m/s normal to the stone was modeled impacting the stone. In this case alone, the lithotripter shock wave was not modeled; only the stress induced by direct impact of the fluid jet on the stone was calculated. This jet is a simplified model of the complex cavitation process, but it is intended to give an approximation to the localized stress created in cavitation collapse. Cavitation Test 3 was simulated with the stone in glycerol ($\rho=1260$ kg/m³, $c_l=1980$ m/s) and with the stone in water. Both showed similar stress concentration at the cracks. Results of the stone in water are shown for simpler comparison to the other figures.

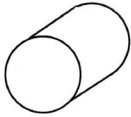
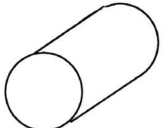
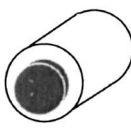
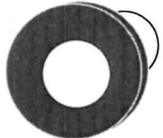
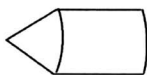

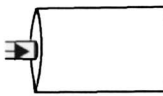
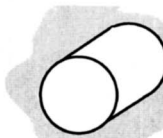
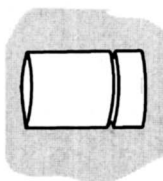
III. MATERIALS AND METHODS

Experiments were conducted in the water bath of a research lithotripter³⁶ modeled after the unmodified (80 nF capacitor) Dornier HM3 electrohydraulic lithotripter (Dornier GmbH, Germany). The reflector was mounted in the tank so that the acoustic axis was horizontal, normal to gravity. Experiments were conducted at 1-Hz repetition frequency and 18 kV charging potential. Room temperature water was filtered through 10 μ m pores before filling the tank and conditioned to 600 μ S/cm and a 25%–30% gas saturation level. Refurbished electrodes (Service Trends, Kennesaw, GA) were used after conditioning with 150 shock waves and were replaced after 2000 shock waves.

Model stones were made from Ultracal-30 (U30) gypsum (United States Gypsum, Chicago, IL). The only modification to the recipe defined by McAteer *et al.*¹⁵ was the use of a plastic mold with pieces that were separated to remove the stones rather than using chloroform to dissolve plastic molds [Fig. 5(a)]. As described previously,¹⁵ the U30 gypsum was mixed for 10 min, poured into molds, and allowed to solidify under water for 24 h. Also as described previously,¹⁵ the gypsum settled some in formation and the lower surface of the stones was slightly harder than the upper surface of the stone. The stones were stored under water and then were removed briefly to place them in the lithotripter bath. Separate stones were dried and resubmerged for 48 h and produced statistically the same results as stones that were never dried. All stones were used within two weeks of preparation.

To test the nine hypotheses listed in Table I, stones of the shapes and dimensions described in Table I were made.

TABLE I. Description and illustration of the numerical tests of the nine hypotheses. Dark objects are acoustically reflective barriers. The proximal face, where the shock wave enters, is circular and on the left facing to different degrees out of the page.

Test	Location and amplitude of σ_{\max} were calculated for	Illustration
Spallation Test #1	stones 6.5 mm in diameter, 8 mm long and cylindrical in shape (standard stones).	
Spallation Test #2	stones of lengths 8-18 mm.	
Spallation Test #3	standard stones with an acoustically reflective disk (1 mm thickness, diameter 4.5 mm) centered on the proximal face of the stone.	
Squeezing Test #1	standard stones with an acoustically reflective disk (1 mm thickness, inner diameter 6.5 mm, outer diameter 25 mm) placed around the proximal face of the stone, leaving the proximal face exposed.	
Squeezing Test #2	standard stones with a conical point on the proximal or distal third of the 8 mm long stone.	
Squeezing Test #3	standard stones with an acoustically reflective disk (1 mm thickness, diameter 6.5 mm) centered on the proximal face of the stone.	
Cavitation Test #1	a water jet (1-mm diameter, 100 m/s velocity) impacting the proximal face of the stone, normal to the face along the axis of the stone.	
Cavitation Test #2	standard stones in glycerol.	
Cavitation Test #3	standard stones in glycerol with a 0.5 mm V-shaped groove encircling the stone either 4 mm, 3 mm or 2 mm from the distal end.	

All cylindrical stones were positioned in the lithotripter with the hard surface (the lower end in preparation) facing the shock source. In Squeezing Test 2, the conical point was the hard surface and pointed either toward or away from the source. In Cavitation Tests 2 and 3, stones were dried for 1 week, placed in 2 mm of glycerol for 1 day to permit wicking into the stone, and then submerged in glycerol for a week. In Cavitation Test 3, a razor blade and a plastic stone holder were used to score a groove encircling stones 2, 3, or

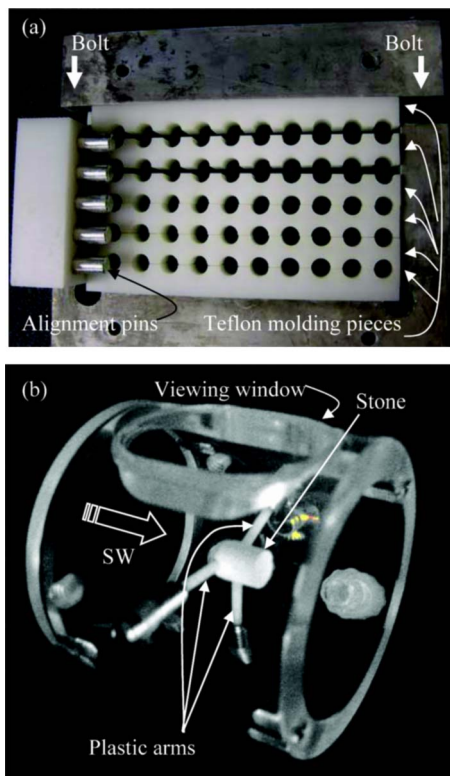


FIG. 5. (Color online) Photographs of the plastic molds used here to form U30 stones (a) and of the holder used to position the stones in the focus of the lithotripter (b). Molds had six white Teflon™ pieces aligned by pins and held in an aluminum frame closed by bolts. The holder had three spring-loaded arms to hold the stone repeatedly but with little interference to the SW.

4 mm from the distal end. The groove was nearly triangular in cross section with a 0.5 mm depth and maximum width of 0.5 mm. In Spallation Test 2 and Squeezing Test 3, the stones were dried for 2 days; a 1-mm-thick corprene disk was glued with epoxy on the proximal face of the stone and allowed to dry for 1 day; and then stone and disk were submerged in water for 1 week. In Squeezing Test 1, a 1-mm-thick corprene baffle was fit without glue around a wet stone. SW pressure transmission through the corprene measured by hydrophone was less than 5%. A number of stones, N , were tested for each experiment, and the number of SWs to fracture were recorded for each stone. Average number for several stones is presented as mean \pm standard deviation.

Stones were fixed axisymmetrically in the acoustic field with the proximal face at the external focus of the lithotripter. The specially designed stone holder was a 5-cm-diam polycarbonate ring with three spring loaded plastic arms that held the proximal edge of the stone with repeatable force [Fig. 5(b)]. The 2-mm-diam arms could be mounted at two positions along the 5 cm length of the holder (4 and 25 mm from the holder aperture). For Cavitation Tests 2 and 3, the holder was capped with foodservice plastic wrap (25 μ m high density polyethylene) and filled with glycerol. Trapped air bubbles were removed through ports in the holder. For the glycerol experiments only, the stone was held with the arms 4 mm from the plastic wrap in an effort to minimize the length of the path through the glycerol, which is more attenu-

ative than water. Glycerol has been used by other researchers to suppress cavitation to investigate comminution mechanisms in SWL.^{20,22}

A CCD camera (Sony CCD-IRIS, Nikon 28-80 lens) mounted outside the acrylic water-filled lithotripter tank recorded movies to laptop computer (ULead card and software, Torrance, CA). The number of SWs to fracture and the position of this fracture along the length of the stone were recorded. The position of the break was also measured from the recovered fragments. The experimental end point was detecting fracture or completing a fixed maximum number of SWs without detecting fracture. The number was fixed for each test but varied from 200 to 250 to 300 between tests. Specific limits are listed with the results.

IV. RESULTS

A. Mechanism described by the numerical model

Figure 6 includes a sequence of images showing the shock-wave-induced maximum principal stress within a U30 stone at specific times. The corresponding time is written in the upper right corner of each frame. At $t=0$ a longitudinal wave propagating in water approaches the stone. Then it enters the stone ($t=1 \mu$ s) and moves ahead of the shock wave in water, because the longitudinal speed in the stone is higher than the sound speed in water. When this longitudinal wave reaches the back end of the stone, it reflects and inverts ($t=4 \mu$ s), creating a thin vertical region of tensile stress indicated by the dashed arrow. This process is called spallation. The region is faint indicating low tensile stress, and the stress does not change greatly over the distal third of the stone. Following the longitudinal wave is a conical wake, compressive in the water and tensile in the stone (marked by arrows at $t=3 \mu$ s) that is generated at the surface of the stone, where the longitudinal wave travels faster than the shear wave in the stone and the sound wave in water and therefore creates a “supersonic” source at the stone surface. Traveling at the sound speed in water along the stone surface and encircling the stone is the shock wave (marked by dotted arrows at $t=1 \mu$ s), and it creates squeezing. The frame at 2μ s yields little time for dynamic wave effects to develop and is therefore the best frame to compare to the static idea of squeezing. In this frame the stress due to squeezing is low amplitude and localized near the surface of the stone. Shear waves generated at the proximal corners of the stone (shown by solid arrows at $t=4 \mu$ s), track the shock wave propagation along the surface of the stone, and focus in the distal half of the stone ($t=5 \mu$ s). Because the shear wave speed in the stone is close to the sound speed in water, the squeezing wave reinforces the shear wave and this shear wave adds to the weaker stress due to spallation to create the highest tensile stress within the stone. The peak σ_{\max} is 100 MPa, is on axis, and is 3.5 mm from the distal surface.

This result of the model can be termed “dynamic squeezing.”¹⁸ Here, the predicted process is labeled “full model.” The peak σ_{\max} occurs 3.5 mm from the distal end on axis. The shortest route to the stress release of the stone surface is in the radial direction. Thus, an orthogonal fracture at 3.5 mm is the most logical interpretation. The modeled

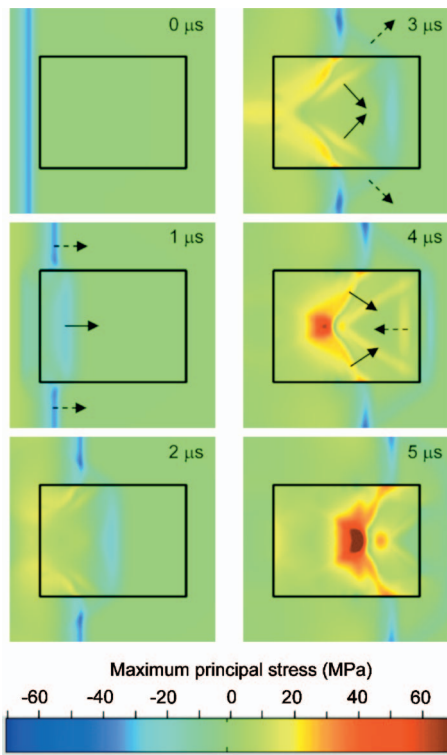


FIG. 6. Calculated results showing the maximum principal stress σ_{\max} in a slice of the stone in a time sequence. The stress σ_{\max} is plotted on a fixed scale blue -70 MPa to red $+70$ MPa, where minus indicates compression. In the on-line version color images are used on a scale blue -70 MPa to red $+70$ MPa. The SW contacts the stone at $t=0$. The arrows in some of the frames indicate direction of propagation of specific waves, with each arrow starting at the corresponding wave front. At $t=1 \mu\text{s}$, the solid arrow represents the compression longitudinal wave in the stone, and two dotted arrows outside the stone show the compression associated with the shock wave propagating in liquid. This wave gives rise to the dynamic squeezing effect. At $t=3 \mu\text{s}$, arrows show two leaky waves that are generated on the stone surface by the longitudinal wave propagating inside the stone: The dotted arrows show the divergent conical wave front of a pressure wave in water and the solid arrow indicates the convergent conical wave front of a shear wave in the stone. At $t=4 \mu\text{s}$, solid arrows start at the wave front of the convergent shear wave that is generated at the proximal corner of the stone and reinforced by the longitudinal wave propagating in water (shown by dotted arrow in $1 \mu\text{s}$ frame), this wave creates the highest tensile stress and can be interpreted as dynamic squeezing. The dotted arrow at $t=4 \mu\text{s}$ shows a longitudinal wave of tension that appears because of reflection of the compression wave from the distal end of the stone; this wave is associated with the “spallation” mechanism. The region of high tension seen at $t=5 \mu\text{s}$ in the central part of the stone is a result of the shear dynamic squeezing wave with little contribution from the longitudinal spallation wave.

time sequence (Fig. 6) illustrates that spallation and squeezing are present, but the shear wave initiated by the corners of the stone and driven by the squeezing wave traveling along the stone (dynamic squeezing) leads to the greatest stress. In the Sec. IV B, tests of the roles of these individual mechanisms and the interpretation of the simulation are reported.

B. Test of mechanisms

The results are summarized in Table II. Data were found to support and to contradict each mechanism. However, the process described by the linear elastic model consistently explained the results.

TABLE II. Summary of results: A plus sign indicates support of a mechanism, and a minus sign indicates contradiction of a mechanism. Results do not support any one of the three mechanisms completely, but the results are consistently explained by the linear elastic model.

Test	Spallation	Squeezing	Cavitation	Full model
Spallation Test 1	+			+
Spallation Test 2	-			+
Spallation Test 3	-			+
Squeezing Test 1	-	+		+
Squeezing Test 2		-		+
Squeezing Test 3		-		+
Cavitation Test 1			-	
Cavitation Test 2			+	
Cavitation Test 3			+	+

If spallation is the sole mechanism, stones will fracture at the distal end as shown in Fig. 2 (Spallation Test 1): All standard stones fractured in two at the distal end (Fig. 2) with what has been termed classic spall fracture or spalling.¹⁶ Standard stones yielded a peak σ_{\max} of 100 MPa, 3.5 mm from the distal surface (modeling), and fractured normal to the cylinder axis after 45 ± 10 SWs ($N=10$) at 3.6 ± 0.2 mm from the distal surface (experiment). Location of fracture agreed well with the location of calculated maximum tension.

This result is the most compelling evidence for spallation. The fracture location is in excellent agreement with the distance $l \approx 3$ mm from the distal end that was predicted for a plane wave in Sec. I. The location is also in good agreement with the broad location of the maximum stress due to spallation seen in the simulation. The region is broad because the negative tail of the shock wave is long.

However, when the model was used to track stress produced only by the longitudinal wave and its reflection, what we have defined as spallation, the maximum tension is much lower, less than 50 MPa. In fact, according to the modeling, the true maximum stress induced by reflection of the longitudinal wave occurs within 1 mm of the distal end and does not exceed 20 MPa. The reason is a shortening of the longitudinal wave due to diffraction at the stone edges. Thus, the full model predicts the location of maximum stress that agrees well with the location of fracture, and the fracture looks like spallation. But the model indicates that the spallation mechanism is not solely responsible and contributes only a small portion of tension where the fracture occurs.

If spallation is the sole mechanism, stones of different length will fracture the same distance from the distal end (Spallation Test 2): Although stones of different lengths broke with classic spall fracture, fracture in longer stones occurred farther from the distal end. The result contradicted spallation. Figure 7 shows the results. Although the predicted location of maximum tension due to spallation is constant in all stone lengths, fracture was farther from the distal end in longer stones. The result that fracture distance increased with stone length was also observed by Xi and Zhong¹⁴ with larger cylindrical stones.

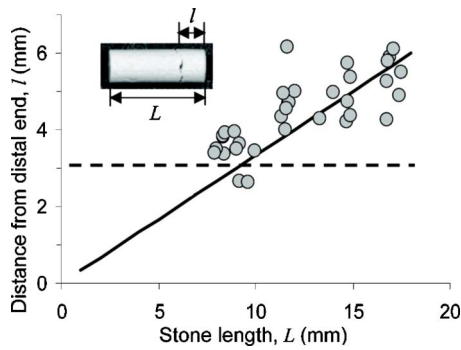


FIG. 7. (Color online) Plot of the distance, l , between the fracture and the distal end vs stone length, L . The fracture occurs farther from the distal end for longer stones whereas spallation should occur repeatedly at the same distance, 3.1 mm, based on only the shock wavelength (dotted line). The solid line corresponds to the distance $l=L/3$.

Figure 7 shows fracture occurred consistently approximately 1/3 of the length from the distal end. Calculated peak σ_{\max} did the same. This one-third point is the location where the shear wave traveling at 1330 m/s meets the reflected longitudinal wave traveling at 2630 m/s. The constructive interference of these two waves produced the peak σ_{\max} as seen in Fig. 6 ($t=5 \mu\text{s}$). The simulations show that both the reflected wave and the focused shear wave maintain a level amplitude for several millimeters around the one-third point.

If spallation is the sole mechanism, blocking transmission of the SW through most of the proximal face will increase the number of SWs to fracture (Spallation Test 3): In the corresponding experiment a 4.5 mm corprene disk was placed on the proximal surface of the stones and prevented the longitudinal SW, responsible for spallation, from entering the stone, yet stone fracture was unchanged with and without the disk, which indicates the fracture mechanism was not spallation. With the shield in place it took 50 ± 20 SWs ($N=8$) to break the stone and the fracture was 3.5 ± 0.1 mm from the distal end, which was not significantly different from the case without the baffle. Comparison of Fig. 6 and the left column of Fig. 8 shows that although the longitudinal wave is attenuated by the small proximal disk, the location and amplitude of peak σ_{\max} were little affected. Calculations, both with and without the baffle, yielded peak σ_{\max} equal to 100 MPa at distance 3.5 mm from the distal end. Based on Spallation Tests 1–3, the fracture in these experiments does not appear to be due to spallation.

If squeezing is the sole mechanism, blocking transmission of the squeezing wave will increase the number of SWs to fracture (Squeezing Test 1): The result of the corresponding test supports squeezing. The baffle ringing the stone's proximal edge blocked the squeezing wave, and the stones did not fracture. The baffle did not cover the proximal or distal faces of the stone but presented a barrier to acoustic waves traveling in the water along the stone. The right column of Fig. 9 shows the calculations. The proximal baffle significantly reduced stress deep in the stone, and the stress produced with the distal baffle was very similar to the case without a baffle (Fig. 6). Correspondingly, no stones with the proximal baffle fractured before the maximum number of applied shock waves, 300, of this experiment ($N=3$). Stones

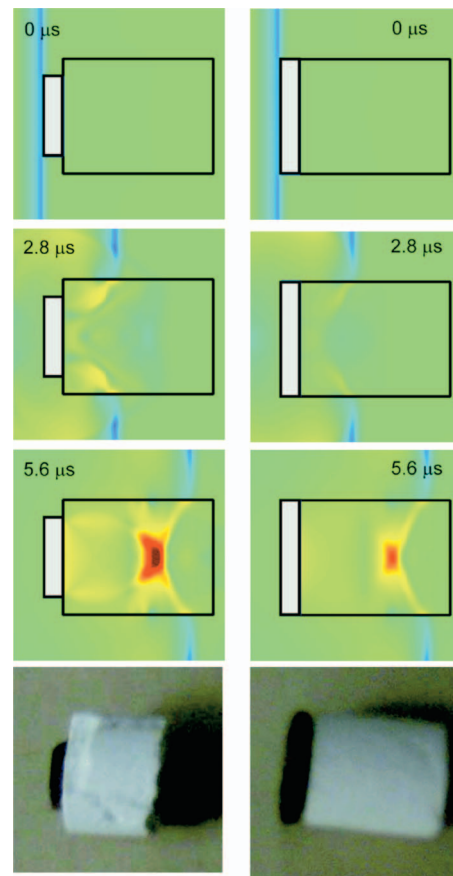


FIG. 8. The stress field calculation for Spallation Test 3 (left) and Squeezing Test 3 (right), where a small reflective disk is positioned on the proximal face of the stone to prevent transmission of the longitudinal wave responsible for spallation from entering the stone. Note no vertical longitudinal wave front is seen entering either stone. When the disk does not cover the proximal edge (disk 4.5 mm diameter, left) the stress pattern and amplitude does not differ significantly from Fig. 6, the maximum stress field without the disk. The calculation indicates spallation does not contribute significantly to the stress in the U30 stone. When the disk covers the entire front surface (disk 6.5 mm diameter, right), stress is still present inside the stone but at reduced amplitude. The result is not explained by static concept of squeezing. The photographs show the fractured stone with the small disk and a still intact stone with the large disk.

broke in 40 SWs with the distal baffle which was not statistically different from the results with no baffle.

The result indicates the squeezing wave is an important contributor; however, the simulations (Fig. 6) indicate that the maximum stress grows over time, which is not what would be expected of the static model of squeezing. Unlike a static field induced by hoop stress, the dynamic stress field in the simulations shows a shear wave generated at the corners of the stone and focusing toward the distal axis of the stone. The shear waves appear to be reinforced by the squeezing wave traveling along the edge of the stone at nearly the same speed as the shear wave speed. Thus, the mechanism is more complicated than and differs from the quasistatic squeezing mechanism proposed by Eisenmenger,¹⁰ but the source is the wave encircling the stone in both cases.

If squeezing is the sole mechanism, the shape of the tip or the tail of the stone will not alter the number of SWs to fracture (Squeezing Test 2): The result of this test did not support squeezing. Although the squeezing wave was little

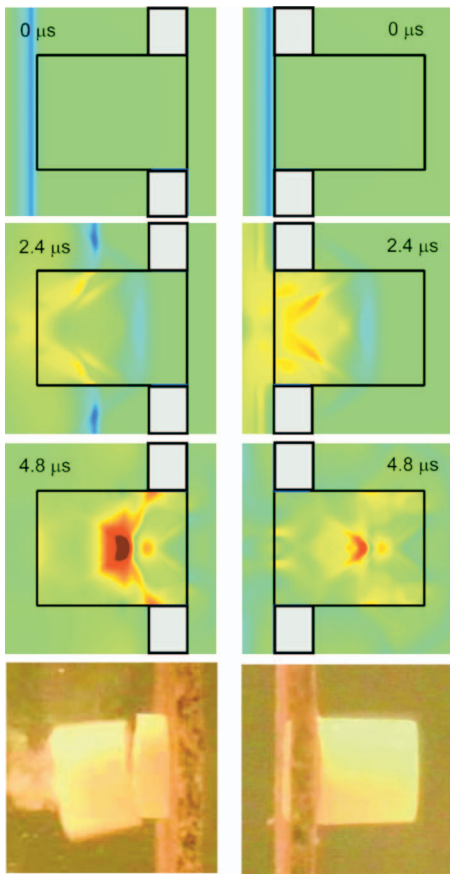


FIG. 9. Comparison of the stress field calculated for Squeezing Test 1 with a reflective baffle around the distal face (left) and proximal face (right) of the stone. The distal baffle case is little different from the no baffle case in Fig. 6. Adding the baffle on the proximal face blocks the squeezing wave and significantly reduces the stress particularly at the distal end of the stone. Thus inhibiting the squeezing wave, for example with a narrow focus, reduces the stress induced in the stone. The images at the bottom are photos of the stones taken during shock wave application. The 1-mm-thick baffle was made of corprene. The photograph on the left was taken at the time of fracture.

changed by the shape of the stone, stones with a proximal conical point required many more SWs to fracture than standard cylindrical stones or stones with a distal point. The stress induced by squeezing in conical stones is the same as in the cylindrical stones since it depends only on the SW amplitude in the water. Figure 10 shows the results of simulation and the images after fracture. With the conical tip on the proximal side, predicted stresses within the stone are very low, and no fracture was observed after 200 SWs ($N=3$), which was the maximum number applied. Although the distal end is cylindrical, the conical tip increases significantly the number of SWs required to fracture the stone. The time sequence of the simulations in Fig. 10 compared to those in Fig. 6 reveals that the tapered conical point did not produce a strong and focused shear wave as was generated at the corners of the blunt end of the cylindrical stone. High stresses were calculated on the distal surface and after ~ 25 SWs a crater 4 mm in diameter and <1 mm deep formed. With the tip on the distal end, high stresses, produced by the shear wave generated at the blunt proximal face, were calculated in the conical region, and the conical section fractured after 40 SWs.

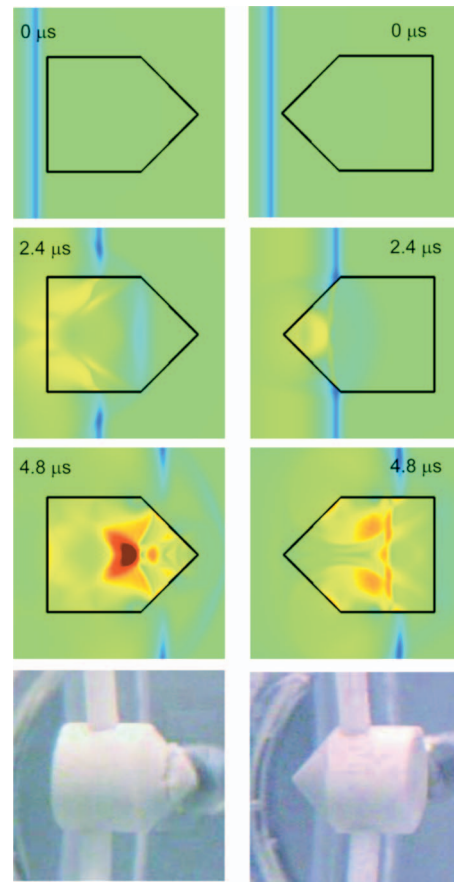


FIG. 10. The stress field calculated for a conical stone with the point distal (left) and proximal (right). The squeezing wave is unaffected in each but the stress is much less with the proximal point. The difference is that the proximal point does not create a strong shear wave, because it does not contain a sharp corner. The result with the distal point is little different from the cylindrical case Fig. 6. Focusing of the shear wave in the cylindrical and the distal conical cases is responsible for the peak tension. The stone in the left photograph shows fracture at the location of σ_{\max} , and the right stone did not fracture.

If squeezing is the sole mechanism, blocking the entire proximal face of the stone will not alter the number of SWs to fracture (Squeezing Test 3): The result of this test did not support static squeezing but supported that the fracture was caused by the shear wave initiated at the proximal corners and strengthened along the side surface of the stone by the liquid-borne lithotripter shock wave. With the whole face covered by a corprene disk, low stresses were predicted in the stone, and stones broke after 212 ± 53 SWs ($N=8$) including three cases where the stone had not broken after 250 SWs, the maximum in this experiment. The distal third of the stone also did not break cleanly from the stone; it splintered into about three pieces. The squeezing wave was largely unaltered as diffraction at the disk is small, but many more SWs were required to fracture the stone, because the shear wave was suppressed.

As a whole, these six tests are in agreement with simulations by the model and the description of the mechanism of creating maximum stress in the stone provided by the model. In the standard stone (Fig. 6, $t=5 \mu\text{s}$), the peak σ_{\max} was in the distal end where the fracture occurred. Stress due to spallation was calculated to be low, but added to the primary

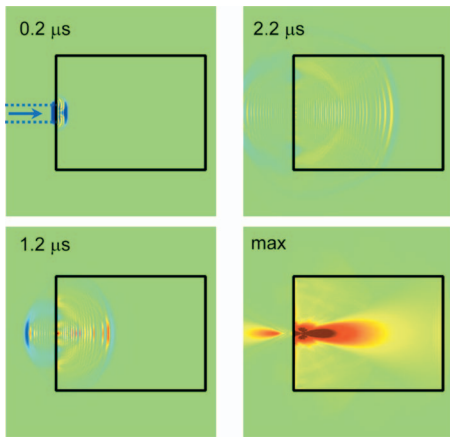


FIG. 11. Maximum principal stress induced by a 1-mm-diam fluid jet impacting upon the U30 stone surface at 100 m/s in a simulation of the fluid jet impact by a collapsing cavitation cloud as seen in Fig. 4(a). It is seen that the jet generates spherically divergent longitudinal (faster) and shear waves (slower) waves in the stone. The bottom-right image represents absolute maximum stress throughout time, the so-called max stress field. Stress is high but localized to the region of impact. Little stress is induced in the distal end where fracture occurred. However, cavitation-induced cracks in the surface may be critical to seeding fracture.

mechanism, which was dynamic squeezing where the shear wave focused from the corner of the proximal face and was reinforced by the squeezing wave. However, cavitation, likely present in the experiment but not present in the model, was not considered.

If cavitation is the sole mechanism, jet impact will produce high stress in the region of fracture (Cavitation Test 1): Although from the first few SWs, experiments showed pits on the proximal and distal surfaces, which is indicative of cavitation, simulation of a cavitation jet impact did not yield high stress at the distal end of the stone where fracture occurred. In Fig. 11 only, the model was used to simulate the force of a 100 m/s water jet (1 mm in diameter) impacting the stone. The result seen in Fig. 11 is that high maximum tension was localized to the region of jet impact. Significant stresses did not appear in the distal portion of the stone except on the distal surface. These distal stresses were due to surface shear waves traveling the surface of the stone and refocusing on the distal surface. As shown previously,^{12,13} the stress of impact in the stone acts as a point source, and losses due to divergence within the stone rapidly weaken the wave. Figure 11 shows some numerical dispersion, and a sufficiently small grid was not obtained to remove it. The dispersion weakens the wave artificially; nevertheless, there was no evidence that further refining the grid would reveal significant stress across the distal third of the stone. From this result, it is apparent cavitation contributes to the pitting erosion on the surface of the stone (Fig. 2) but does not appear to contribute directly or strongly to the fracture, because it induces no strong stress in the region of the crack.

If cracks formed by cavitation are significant in fracture, stones in a cavitation suppressing medium will have a higher number of SWs to fracture than stones in a cavitating medium (Cavitation Test 2): The corresponding experimental results supported that with cavitation suppressed stones took longer to fracture. Standard stones in glycerol required

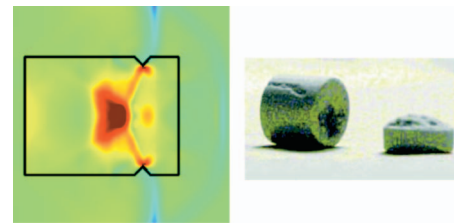


FIG. 12. A stone etched 2 mm from the distal end fractures in a conical shape (right) as illustrated by the modeled peak stress field at $t=5 \mu\text{s}$ (left). Stress concentrations appear at the tip of the etched cracks. The result indicates fractures grow between the point of maximum stress and surface cracks as may be generated by cavitation as illustrated in Fig. 4(b).

127 ± 57 SWs ($N=8$) to break. Vakil *et al.*²² also found many more SWs were required to fracture stones in glycerol. Although the previous test showed the cavitation collapse might not induce significant stresses within the stone, this test result indicates that surface pitting is important in fracture.

If cracks formed by cavitation are significant in fracture, stones with surface cracks but in a cavitation suppressing medium will have the same number of SWs to fracture as stones initially without surface cracks in a cavitation supporting medium (Cavitation Test 3): This test was positive. Stones with the etched band 2 mm from the distal surface required 17 ± 6 SWs ($N=8$) to break in glycerol. The fractures were conical as might be predicted by the calculated peak maximum tensile surface, a two-dimensional view of which is shown in Fig. 12. Thus with cavitation suppressed, the stones did not break unless an etched band (representing cavitation damage) was present, and the fracture pattern was predictable with the model.

When the etched band was placed 3 or 4 mm instead of 2 mm from the distal end, fracture was not as rapid. However in water, 17 ± 8 SWs ($N=5$) were required to break a stone with an etched band at 4 mm, which is not statistically different from the etched stone in glycerol. The sensitivity to location of the etch is likely due to the faster sound speed in glycerol, but the similarity in number of SWs to fracture indicates that glycerol had little effect other than to reduce cavitation. Simulations in glycerol also showed little effect, but a slight reduction in peak σ_{max} due to (1) loss at the slight acoustic impedance mismatch between water and glycerol and (2) the mismatch, and therefore reduced reinforcing, between the sound speed in glycerol and the shear wave speed in the stone.

C. Summary of results

Figures 13 and 14 show a summary of calculated results for some of the cases. Figure 13 shows peak maximum tensile stress that occurred at anytime during the simulation at every point in the field, the max stress field. Figure 14 shows an axial plot of these max stresses. The left column of Fig. 13 and the lines labeled a, b, and d in Fig. 14 show how little the stresses were changed by blocking the longitudinal wave from entering the stone or altering the distal end of the stone. In addition, stress is concentrated at the tips of cracks (top

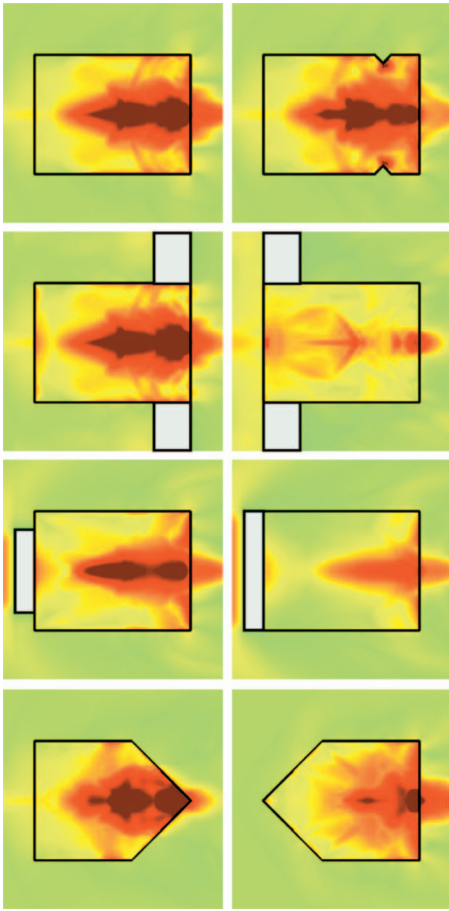


FIG. 13. Distribution of the absolute maximum throughout time of the maximum principal stress (tension) in various test stones. The max stress field is little changed by blocking the longitudinal wave entering the stone or altering the distal end of the stone as in the left column. In addition, stress is concentrated at the tips of cracks (top right). However, blocking the “squeezing” wave or preventing creation of a shear wave at the corners of the proximal face significantly reduces the stress (lower three frames in the right column). In addition, the elastic waves in the stone create high negative pressure (~ 50 MPa) in the liquid near the proximal and distal surfaces of the stone. Cavitation may be expected in these regions and is indeed observed (Ref. 26).

right in Fig. 13). However, the lower three frames in Fig. 13 and the lines labeled c and e in Fig. 14 show how dramatically the stress is reduced by blocking the “squeezing” wave or preventing creation of a shear wave at the corners of the proximal face. The lower right frame in Fig. 13 indicates that the squeezing wave is most important in creating the stress in that although the proximal corners are smooth and not abrupt, high stress is created and occurs near the distal end as the squeezing wave must travel over the length of the stone to generate the reinforcement and focusing.

In addition to the stress field in the stone, the negative pressures in liquid are of interest. The negative pressure of the planar shock wave is -10 MPa and is not particularly noticeable in Fig. 13. Instead the elastic waves in the stone generate negative pressures greater than -10 MPa in the fluid around the stone.²⁶ At the proximal and particularly the distal end of the stones negative pressure near -50 MPa is calculated and this is where particularly large and long-lasting cavitation bubbles are observed (Fig. 4).²⁶ In addition,

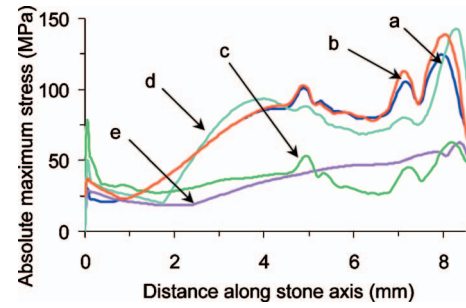


FIG. 14. Distribution of the absolute maximum throughout time of the maximum principal stress (tension) along cylindrical stone axis in various test conditions: (a) standard stone, (b) baffle encircling distal end, (c) baffle encircling proximal end, (d) 4.5 mm disk on the proximal face, and (e) 6.5 mm disk on the proximal face. Blocking the longitudinal wave responsible for spallation only minimally reduces the stress, (d). Blocking generation of the shear wave (e) from the proximal corners of the stone or blocking the squeezing wave (c) that drives the shear wave results in a significant reduction in stress in the stone.

tion, faint but still strong negative pressure can be seen ringing the stone on the distal end, which presumably contributes to the band of bubbles encircling the stone.²⁹

V. DISCUSSION AND CONCLUSIONS

A new mechanistic description of stress and fracture in cylindrical U30 stones in lithotripsy was reported. The description is that shear waves generated at corners in the boundary of the stone are reinforced by the SW in water traveling along the surface of the stone and focus to generate the highest stress in the distal end of the stone. It was argued that a fracture plane results between the maximum stress and the stone surface. The description is the result of calculation based on linear elasticity theory. Although some in the lithotripsy community have been content that energy density (temporal and spatial integral of the pressure squared divided by the focal beam width)³⁸ of the conventional lithotripsy shock wave correlates with stone comminution,¹⁶ this model shows how the energy is applied is important and leads to different mechanisms of action. Long ago, Griffith³⁹ introduced an energy concept to fracture mechanics that we apply here to kidney stones and that states that the fracture growth depends on the elastic energy (associated with tension) applied to the material. However, the important energy is that associated with the tension in the stone and not the initial energy in the shock wave applied to the stone. The tension in the stone was adequately described by the model but is not simply related to the SW energy or energy density: it depends on the shock waveform as shown by Sapozhnikov and Cleveland¹⁸ and on beamwidth as shown here as well. If the beamwidth of the lithotripter is narrower than the stone then dynamic squeezing—the dominant mechanism in this study—cannot contribute.

A series of experiments tested the result of the theoretical model versus already defined mechanisms—spallation, squeezing, and cavitation—of inducing stress in the stone. Some test results could be explained by spallation or squeezing, but other tests could not. The results of the model were consistent with all the tests. A SW beamwidth broader than the stone was critical to maximizing the stress in the stone.

Test results did not support that cavitation on the proximal end generated stress that led to fracture seen on the distal end of the stone. However, results did support that cavitation pitting on the surface led to stress concentrations from which fractures grow. It should be noted that multiple localized stresses resulting from many cavitation bubbles along the surface of the stone as seen in experiments²⁶ were not simulated and could possibly sum to generate considerable stress deep within the stone.

The mechanisms were specifically and rigorously defined. Although the model includes shear in general, the mechanism related to shear discussed here was shear waves generated at the boundary of the stone. Spallation is the creation of tension due by the interference of the longitudinal wave and its inverted reflection. Squeezing is a static concept of stress induced by a narrow band of pressure encircling the stone. Others have dismissed squeezing from outside the stone and attributed comminution entirely to spallation by loosely defining spallation as “shear and tear,”¹⁶ in other words all stress within the stone. However, this broad definition of spallation essentially means the comparison could be restated as stress in the stone is more important than stress outside the stone, which is obvious. Our results with the rigorous definition of the mechanisms show that shear waves reinforced by squeezing and to a small extent constructively interfering with the reflected longitudinal wave lead to the maximum stress. The location of this peak maximum principal tensile stress, not the location of the maximum stress of spallation, agrees with the location of the “spall fracture” or fracture in two at the distal end.

Our experiment was also specific. The end point was the first fracture into two pieces of a specific stone, fixed in a specific position, in specific fluid conditions, in a specific lithotripter. The controlled conditions provided for a careful test of the model and of mechanisms of breakage. The excellent correlation of calculated high stress to few shock waves to fracture and the location of high stress to the location of fracture in these controlled tests gives confidence in the model. From here, the use of the model might be extended.

For example, repeated calculations might be used to simulate the comminution process. (It is important to note here that one case of axisymmetric simulations shown in Figs. 6 and 8–10 takes fewer than 10 min on a 2 GHz personal computer, i.e., the modeling is fairly fast.) Our study neglected how the role of each mechanism may change with repetitive shock waves and stone breakage. Appearance of a crack will reflect the shock wave and prevent its propagation deeper in the stone; the stress distribution would then change. In repetitive SW application, cavitation plays two additional roles. With repetitive shock waves especially at fast clinical rates, bubbles do not have sufficient time to dissolve between consecutive shock waves, and absorption and scattering of the acoustic energy by the bubbles can reduce the pressure that reaches the stone.^{31,40–42} Also, cavitation may play an increasingly important role as stones fragment and become smaller.⁴³ Elastic wave propagation is suppressed as stones approach the size of a wavelength, but surface forces, such as generated by cavitation, are not a function of stone size.¹⁸ However, a series of simulations,

where perhaps the SW amplitude is diminished to simulate shielding and stone size is reduced to simulate fragmentation, may reveal how the dominant mechanism changes during treatment.

The model may be used to test the parameter space of stone material, stone shapes, shock wave beamwidths, and more, in ways not reasonable by experiments. It may be gleaned from our results that the shear wave so important in the cylindrical stone would be less important in the spherical stone because shear waves were generated at sharp edges in the stone boundary. Calculations would be further refined by including a simulation of cavitation activity^{31,32} and fracture dynamics.⁶ Currently, simulation could be useful in treatment planning. For example, focal beamwidth, which is adjustable on some current machines, might be changed based on a diagnostic image of the stone and a calculation of the stress produced in the stone. In the future, real-time imaging and simulation could direct changes to the beamwidth or the shock waveform during treatment.

In summary, it was reported that a theoretical model accurately described the physical mechanism leading to observed stone fracture. None of the specific mechanisms, spallation, squeezing, or cavitation, completely described the fracture. The results of the model were more useful than these descriptors.

ACKNOWLEDGMENTS

The authors would like to thank the many members of the Consortium on Shock Waves in Medicine and the Center for Industrial and Medical Ultrasound for discussions, research help, and guidance on this paper. In particular, we would like to thank Professor James A. McAteer, Dr. Yuriy A. Pishchalnikov, and Professor James C. Williams, Jr. (Indiana University School of Medicine) for guidance in preparing U30 stones, Professor Robin Cleveland for collaboration in developing the numerical code, and Fran Olson for design and fabrication of much of the experimental apparatus. The work was supported by NIH Grant Nos. DK43881 and DK55674, NSBRI Grant No. SMS00402, an NIH Fogarty International Research Collaboration Award, an ONR International Field Office Visiting Scientist grant, a CRDF grant, and RFBF grants.

¹K. Kerbl, J. Rehman, J. Landman, D. Lee, C. Sundaram, and R. V. Clayman, “Current management of urolithiasis: Progress or regress?,” *J. Endourol* **16**, 281–288 (2002).

²A. P. Evan, J. A. McAteer, J. C. Williams, L. R. Willis, M. R. Bailey, L. A. Crum, J. E. Lingeman, and R.O. Cleveland, “Shock wave physics of lithotripsy: Mechanisms of shock wave action and progress toward improved SWL,” in *Textbook of Minimally Invasive Urology*, edited by R. Moore, J. T. Bishoff, S. Loening, and S. G. Docimo (Martin Dunitz, London, 2004), Chap. 28, pp. 425–438.

³J. A. McAteer, J. C. Williams, Jr., M. R. Bailey, R. O. Cleveland, and A. P. Evan, “Strategies for improved shock wave lithotripsy,” *Minerva Urol. Nefrol* **57**, 271–279 (2005).

⁴B. Sturtevant, “Shock wave physics of lithotripters,” in *Smith’s Textbook of Endourology*, edited by A. D. Smith (Quality Medical Publishing, St. Louis, 1996), pp. 529–552.

⁵G. I. Barenblatt, “The mathematical theory of equilibrium cracks in brittle fracture,” *Adv. Appl. Mech.* **7**, 55–129 (1962).

⁶M. Ortiz, “Microcrack coalescence and macroscopic crack growth initiation in brittle solids,” *Int. J. Solids Struct.* **24**, 231–250 (1988).

⁷M. Lokhandwalla and B. Sturtevant, “Fracture mechanics model of stone

- commutation in ESWL and implications for tissue damage," *Phys. Med. Biol.* **45**, 1923–1940 (2000).
- ⁸C. Chaussy, E. Schmiedt, D. Jocham, V. Walther, W. Brendel, B. Forssmann, and W. Hepp, *Extracorporeal Shock Wave Lithotripsy: New Aspects of the Treatment of Kidney Stone Disease*, edited by C. Chaussy (Karger, Basel, 1982).
- ⁹M. Delius, G. Heine, and W. Brendel, "A mechanism of gallstone destruction by extracorporeal shock waves," *Naturwiss.* **75**, 200–201 (1988).
- ¹⁰W. Eisenmenger, "The mechanisms of stone fragmentation in ESWL," *Ultrasound Med. Biol.* **27**, 683–693 (2001).
- ¹¹H. Kolsky, *Stress Waves in Solids* (Dover, New York, 1963).
- ¹²G. Dahake and S. M. Gracewski, "Related articles finite difference predictions of P-SV wave propagation inside submerged solids. I. Liquid-solid interface conditions," *J. Acoust. Soc. Am.* **102**, 2125–2137 (1997).
- ¹³G. Dahake and S. M. Gracewski, "Finite difference predictions of P-SV wave propagation inside submerged solids. II. Effect of geometry," *J. Acoust. Soc. Am.* **102**, 2138–2145 (1997).
- ¹⁴X. Xi and P. Zhong, "Dynamic photoelastic study of the transient stress field in solids during shock wave lithotripsy," *J. Acoust. Soc. Am.* **109**, 1226–1239 (2001).
- ¹⁵J. A. McAteer, J. C. Williams, Jr., R. O. Cleveland, J. Van Cauwelaert, M. R. Bailey, D. A. Lifshitz, and A. P. Evan, "Ultrasound-30 gypsum artificial stones for lithotripsy research," *Urol. Res.* **33**, 429–434 (2005).
- ¹⁶J. J. Rassweiler, G. G. Tailly, and C. Chaussy, "Progress in lithotripter technology," *EAU Update Series* **3**, 17–36 (2005).
- ¹⁷W. Eisenmenger, X. X. Du, C. Tang, S. Zhao, Y. Wang, F. Rong, D. Dai, M. Guan, and A. Qi, "The first clinical results of 'wide focus and low pressure' ESWL," *Ultrasound Med. Biol.* **28**, 769–774 (2002).
- ¹⁸R. O. Cleveland and O. A. Sapozhnikov, "Modeling elastic waves in kidney stones with application to shock wave lithotripsy," *J. Acoust. Soc. Am.* **118**, 2667–2676 (2005).
- ¹⁹L. A. Crum, "Cavitation microjets as a contributory mechanism for renal calculi disintegration in ESWL," *J. Urol. (Baltimore)* **140**, 1587–1590 (1988).
- ²⁰C. C. Church, "A theoretical study of cavitation generated by an extracorporeal shock wave lithotripter," *J. Acoust. Soc. Am.* **86**, 215–227 (1989).
- ²¹M. Delius, "Minimal static excess pressure minimises the effect of extracorporeal shock waves on cells and reduces it on gallstones," *Ultrasound Med. Biol.* **23**, 611–617 (1997).
- ²²N. Vakil and E. C. Everbach, "Transient acoustic cavitation in gallstone fragmentation: A study of gallstones fragmented *in vivo*," *Ultrasound Med. Biol.* **19**, 331–342 (1993).
- ²³M. R. Bailey, "Control of acoustic cavitation with application to lithotripsy," Technical Report No. ARL-TR-97-1, Applied Research Laboratories, The University of Texas at Austin, Austin, TX and Defense Technical Information Center, Belvoir, VA, 1997.
- ²⁴X. F. Xi and P. Zhong, "Improvement of stone fragmentation during shock wave lithotripsy using a combined EH/PEAA shock wave generator—in vitro experiments," *Ultrasound Med. Biol.* **26**, 457–467 (2000).
- ²⁵R. O. Cleveland and J. van Cauwelaert, "Fragmentation mechanisms of kidney stones in shock wave lithotripsy can be detected with microCT X-ray imaging," *Proceedings of the Joint German Convention on Acoustics and Congrès Français d'Acoustique (CFA)*, Strasbourg, France, 2004, edited by D. Cassereau and M. Kob, Vol. 2, pp. 981–982.
- ²⁶Y. A. Pishchalnikov, O. A. Sapozhnikov, J. C. Williams, Jr., A. P. Evan, J. A. McAteer, R. O. Cleveland, T. Colonius, M. R. Bailey, and L. A. Crum, "Cavitation bubble cluster activity in the breakage of kidney stones by lithotripter shock waves," *J. Endourol.* **17**, 435–446 (2003).
- ²⁷J. R. Blake and D. C. Gibson, "Cavitation bubbles near boundaries," *Annu. Rev. Fluid Mech.* **19**, 99–123 (1987).
- ²⁸A. Philipp, M. Delius, C. Scheffczyk, A. Vogel, and W. Lauterborn, "Interaction of lithotripter-generated shock waves with air bubbles," *J. Acoust. Soc. Am.* **93**, 2496–2508 (1993).
- ²⁹O. A. Sapozhnikov, R. O. Cleveland, M. R. Bailey, and L. A. Crum, "Numerical modeling of stresses generated by lithotripter shock wave in cylindrical kidney stone," *Third International Symposium on Therapeutic Ultrasound*, Lyon, France, 2004, pp. 323–328.
- ³⁰F. R. Gilmore, "The growth or collapse of a spherical bubble in a viscous compressible liquid," *California Institute of Technology Report No. 26–4*, 1952, pp. 1–40.
- ³¹M. Tanguay and T. Colonius, "Progress in modeling and simulation of shock wave lithotripsy (SWL)," *Fifth International Symposium on Cavitation (CAV2003)*, Osaka, Japan, 2003, <http://iridium.me.es.osaka-u.ac.jp/cav2003/index1.html>; paper OS-2–1–010. Last viewed 1/19/2007.
- ³²E. A. Zabolotskaya, Yu. A. Ilinskii, G. D. Meegan, and M. F. Hamilton, "Bubble interactions in clouds produced during shock wave lithotripsy," *Proc.-IEEE Ultrason. Symp.* **2**, 890–893 (2004).
- ³³R. J. LeVeque, *Finite Volume Methods for Hyperbolic Problems* (Cambridge University Press, New York, 2002).
- ³⁴F. Ebrahimi and F. Wang, "Fracture behaviour of urinary stones under compression," *J. Biomed. Mater. Res.* **23**, 507–521 (1989).
- ³⁵J. Vireux, "P-SV wave propagation in heterogenous media: Velocity stress finite-difference method," *Geophysics* **51**, 889–901 (1986).
- ³⁶R. O. Cleveland, M. R. Bailey, N. Fineberg, B. Hartenbaum, M. Lokhandwalla, J. A. McAteer, and B. Sturtevant, "Design and characterization of a research electrohydraulic lithotripter patterned after the Dornier HM3," *Rev. Sci. Instrum.* **71**, 2514–2525 (2000).
- ³⁷R. O. Cleveland, D. A. Lifshitz, B. A. Connors, A. P. Evan, L. R. Willis, and L. A. Crum, "*In vivo* pressure measurements of lithotripsy shock waves in pigs," *Ultrasound Med. Biol.* **24**, 293–306 (1998).
- ³⁸International Electrotechnical Committee, "Ultrasonics—pressure pulse lithotripters—characteristics of fields," *IEC Standard No. 61846*, 1998.
- ³⁹A. A. Griffith, "The phenomenon of rupture and flow in solids," *Philos. Trans. R. Soc. London, Ser. A* **221**, 163–198 (1920).
- ⁴⁰R. F. Paterson, D. A. Lifshitz, J. E. Lingeman, A. P. Evan, B. A. Connors, J. C. Williams, Jr., and J. A. McAteer, "Stone fragmentation during shock wave lithotripsy is improved by slowing the shock wave rate: Studies with a new animal model," *J. Urol. (Baltimore)* **168**, 2211–2215 (2002).
- ⁴¹O. A. Sapozhnikov, V. A. Khokhlova, M. R. Bailey, J. C. Williams, Jr., J. A. McAteer, R. O. Cleveland, and L. A. Crum, "Effect of overpressure and pulse repetition frequency on shock wave lithotripsy," *J. Acoust. Soc. Am.* **112**, 1183–1195 (2002).
- ⁴²Y. A. Pishchalnikov, O. A. Sapozhnikov, M. R. Bailey, I. V. Pishchalnikova, J. C. Williams, Jr., and J. A. McAteer, "Cavitation selectively reduces the negative-pressure phase of lithotripter shock pulses," *ARLO* **6**, 280–286 (2005).
- ⁴³S. L. Zhu, F. H. Cocks, G. M. Preminger, and P. Zhong, "The role of stress waves and cavitation in stone comminution in shock wave lithotripsy," *Ultrasound Med. Biol.* **28**, 661–671 (2002).